



Mechanical Behavior and Microstructural Characteristics of Ultradeep Tight Carbonate Rocks With Different Burial Depths

Ran Zhang¹, Jianmeng Sun^{1*}, Zhigang Cheng², Bixiao Xin¹ and Hao Chen³

¹China University of Petroleum, Qingdao, China, ²China Petroleum Logging Co. Ltd, Xi'an, China, ³Chinese Academy of Sciences (CAS), Beijing, China

OPEN ACCESS

Edited by:

Gang Lei,

King Fahd University of Petroleum and Minerals, Saudi Arabia

Reviewed by:

Hemin Yuan,

China University of Geosciences, China

Jing Ba,

Hohai University, China

*Correspondence:

Jianmeng Sun
sunjm@upc.edu.cn

Specialty section:

This article was submitted to Economic Geology, a section of the journal Frontiers in Earth Science

Received: 20 January 2022

Accepted: 11 April 2022

Published: 03 May 2022

Citation:

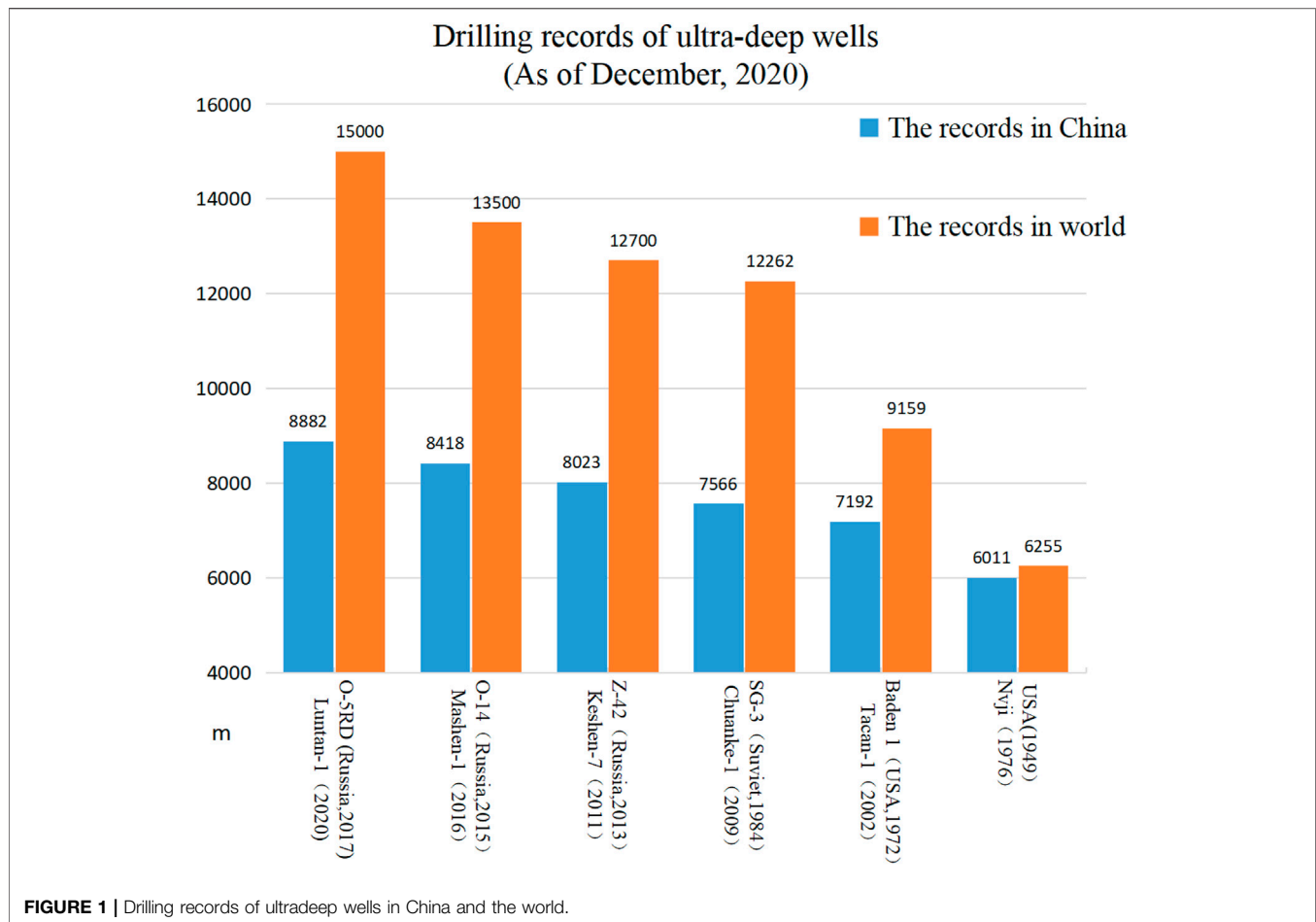
Zhang R, Sun J, Cheng Z, Xin B and Chen H (2022) Mechanical Behavior and Microstructural Characteristics of Ultradeep Tight Carbonate Rocks With Different Burial Depths. *Front. Earth Sci.* 10:858899. doi: 10.3389/feart.2022.858899

The rapid growth in energy demand has placed more attention on the exploration and development of oil and gas in ultradeep reservoirs. However, deep buried rocks in the special “three high” geological environment exhibit significantly different mechanical response characteristics and microstructural features compared with shallow rocks, which requires more targeted experiments and theoretical research. In this work, tight carbonate rocks obtained from five different burial depths ranging from 6077 to 6738 m are used to carry out quasi *in situ* triaxial compression tests under dry and saturated states. Combined with digital rock modeling based on computed tomography scans, the macromechanical responses and microstructural characteristics of the target samples with the variation of depth are analyzed. The results indicate that the long-term strength of deep rocks is much closer to the peak strength than that of shallow rocks, which can reach 94%–99% of the peak strength. The deeper-buried samples exhibit more pronounced plasticity under the same high confining pressure, and their elastic modulus is more likely to be weakened by pore water. Meanwhile, the ratios of residual strength to peak strength increase as the burial depth increases. Interestingly, the samples with weaker structures are more prone to alternate strain hardening and strain softening during the postpeak stage. On the other hand, the distribution of microstructural parameters for different depths is presented to help interpret the mechanical behaviors, and the difference in the dynamic and static elastic modulus of saturation is significantly connected with the mean pore–throat ratios. These results could provide a reference for research on deep rock mechanics.

Keywords: ultradeep rock, different depths, carbonate rocks, digital rock, mechanical parameters, microstructural parameters

1 INTRODUCTION

With the development of petroleum and gas exploitation and the rapid growth in energy demand, more attention has been given to the deep-underground and deep-sea domains (Kang et al., 2010; Li and Feng, 2013; Ranjith et al., 2017; De Santis et al., 2020). Countries have made significant improvements at 6000–10,000 m in technical exploration capabilities as their development priorities focus on the strategic deployment of oil and gas resources. The number of ultradeep wells has increased greatly, and the depth has deepened continuously. In less than 40 years, the world’s deepest



drilling record improved by nearly 6000 m, reaching 15,000 m, and the depth of exploitation in China reached 8,882 m in 2020 (as shown in **Figure 1**). It is worth noting that different countries and institutions do not have a unified definition of “ultradeep”, the Ministry of Land and Resources of China (Wang J. et al., 2013) and the United States Geological Survey (Dyman et al., 1998) defined reservoirs with burial depth greater than 4,500 m as deep oil and gas reservoirs and over 6000 m as ultra-deep oil and gas reservoirs. This definition is adopted in this paper.

The accurate measurement of rock mechanics parameters and the understanding of corresponding mechanical response mechanisms are prerequisites for effective oil and gas exploitation. However, the deep buried rock in the special “three high” (high ground stress, high earth temperature, high karst water pressure) geological environment exhibits different mechanical response characteristics and microstructural features compared with shallow reservoirs (Yang et al., 2014; Vorobiev and Morris, 2019), such as strong rheological properties, the brittleness–ductility transition of the rock, significant time effects, failure mechanisms under high geostress and the mechanisms of disaster occurrence (Pusch, 1993; Malan and Basson, 1998; Malan, 1999; Zhang et al., 2000). These traits make traditional linear elastic longitudinal and transverse wave theory and continuum mechanics, which are widely used in geophysics,

rock mechanics and seismology, unable to accurately predict the mechanical parameters and interpret the experimental results. As a result, engineering demands have prompted deep rock mechanics to become a focus since the 1970s (Kaiser and Cai, 2012; Gong et al., 2018; Wang et al., 2018; Wu et al., 2019). In terms of experiments, Liang et al. (2020) employed a triaxial apparatus under simulated reservoir pressure and temperature conditions to research the creep characteristics of shale in the Cooper Basin at more than 3000 m underground. Tarasov and Randolph. (2008) investigated the impact of the frictionless shear effect of a seismically active gold mine at great depth on the rockburst process. Huang et al. (2020) showed that the mass, longitudinal wave velocity, peak stress and elastic modulus of sandstone at 1000 m deep decreased obviously by 0.43%, 7.87%, 70.20% and 88.10%, respectively, after acid-dry-wet (A-D-W) cycles. Kaiser and Kim. (2015) observed that *in situ* rock strength may be greater than what has been extrapolated from the laboratory; furthermore, they indicated that empirical rock mass strength estimation faces a great challenge in anticipating the actual behavior of brittle rocks during laboratory testing. In strength theory, because the failure of deep rock is no longer controlled by the brittle energy and fracture toughness, the Coulomb-Mohr criterion is invalid, and various nonlinear criteria and unified strength theories of linearity and

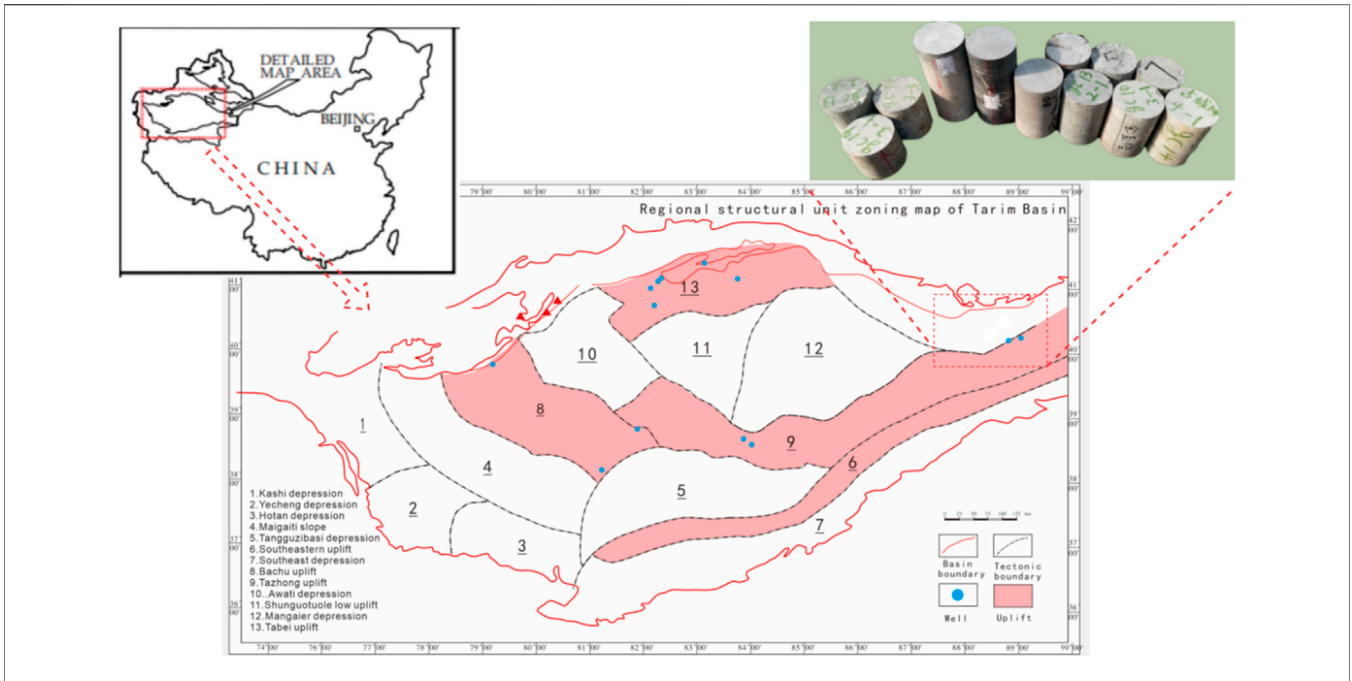


FIGURE 2 | Map of Tarim basin, including a schematic diagram of the full-diameter core sampling location.

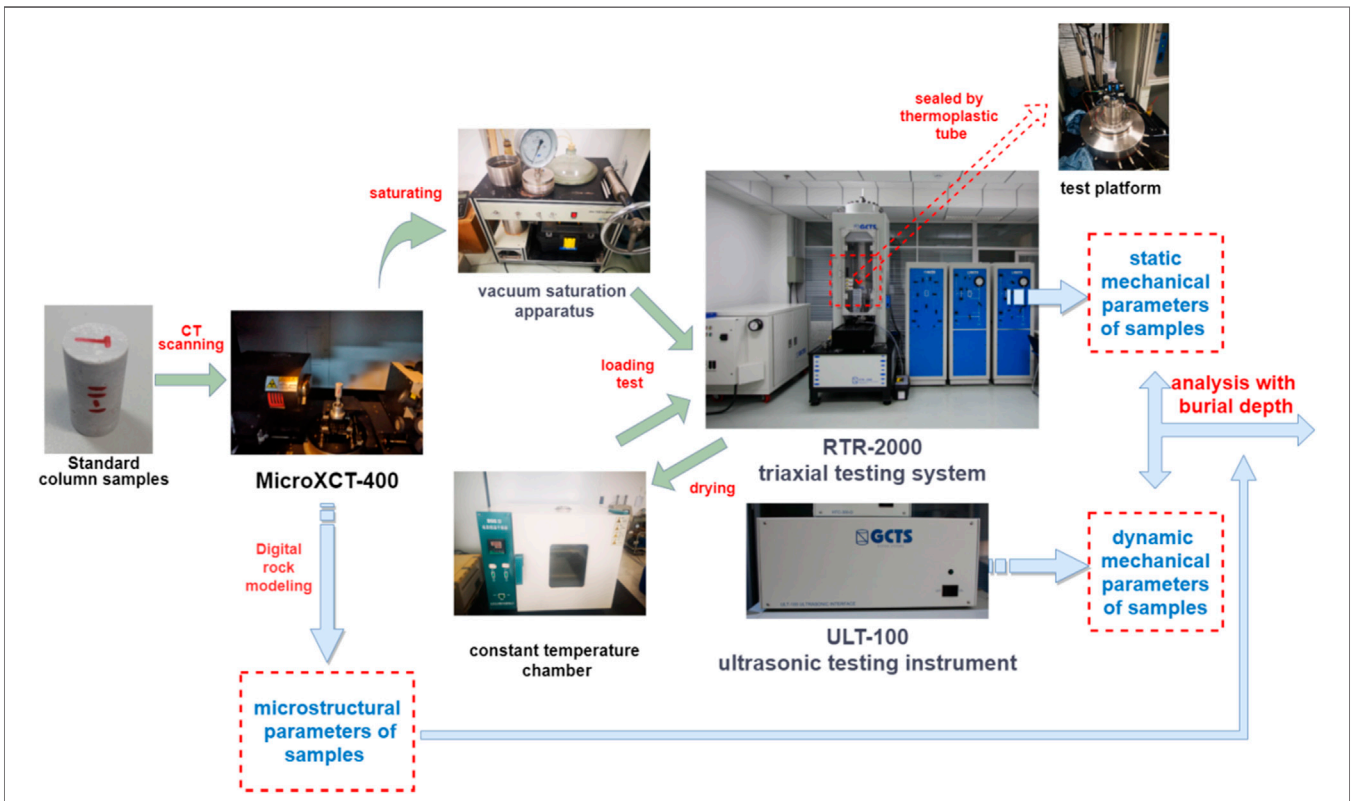
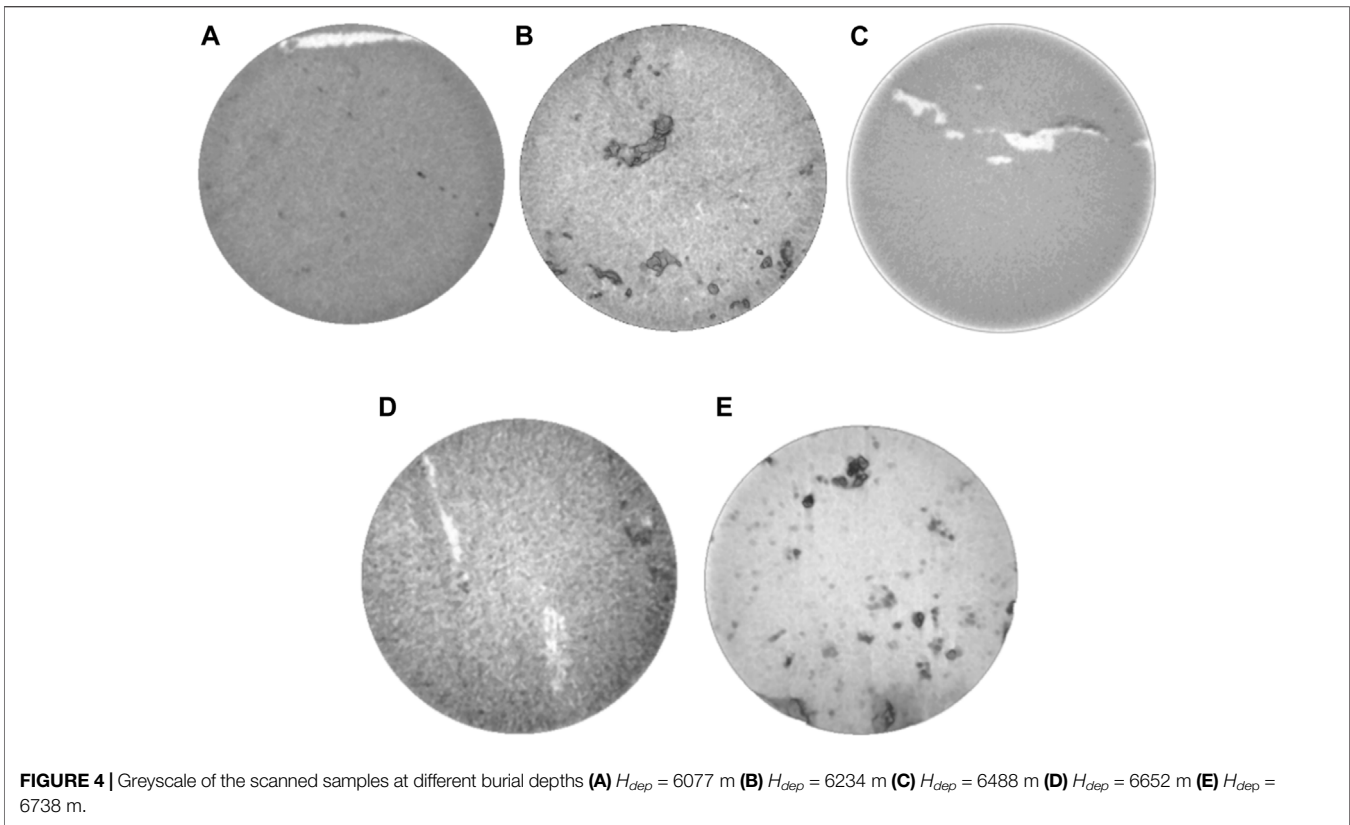


FIGURE 3 | Schematic diagram showing the experimental equipment and procedures.

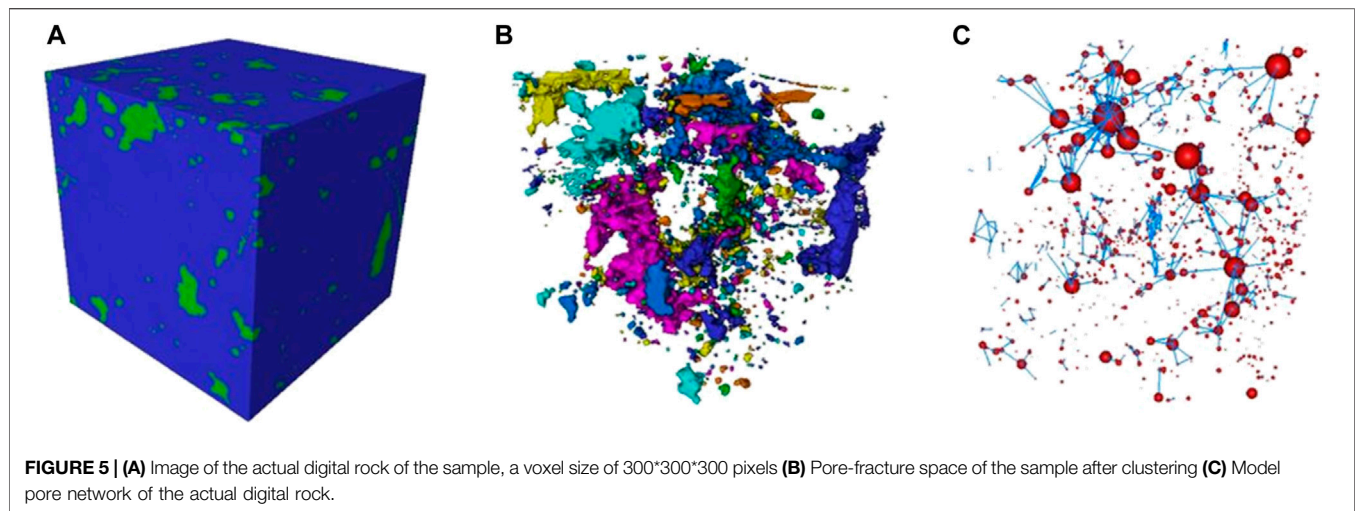


nonlinearity have been developed successively (Zienkiewicz, 1977; Hoek and Brown, 1997; Tzanakis, 1997; Yu et al., 2004). For example, Singh et al. (1989) summarized the rock strength criteria under a lateral stress of 700 MPa and proposed a nonlinear rock strength criterion on this basis.

Although a series of results have been achieved in the field of deep rock mechanisms, there are few basic studies on rock mechanical parameters below 6,000 m and the mechanism of variation with depth. Kang et al. (2019; Peng et al., 2020) researched the variation in static and dynamic mechanical properties of granite with burial depths in the range of 750–1,250 m, and the law of energy evolution in the process of rock failure under different burial depths was discussed; nevertheless, the *in situ* geological conditions of the sample were not fully considered. Xie et al. (2021) tested the mechanical behavior of rocks under *in situ* geological conditions at 10 different burial depths, but the large burial depth span of 1000–6,400 m could make the regular behavior of the variation with depth less obvious. As a rule, the geological conditions become more complex as the depth increases, and the deep scientific phenomena become more obvious; for instance, rockburst, zonal fracture and low-frequency resonance in deep rock mass engineering response become more serious as the depth increases (Li et al., 2020). Furthermore, the precision of the traditional fracture pressure model is still able to meet the engineering requirements above 6,000 m depth for the target area in this paper but has a large error after more than 6,000 m. Therefore, targeted experiments and theoretical studies on

ultradeep rocks, especially *in situ* conditions, appear to be particularly meaningful. These studies also provide calibration and constraints for numerical simulations and petrophysical trend prediction analyses (Tang, 1997; Avseth et al., 2003; Zhu et al., 2012).

On the other hand, the current research on rocks at different depths has been mainly focused on the macromechanical properties and the effects of different confining pressures and temperatures on the mechanical behavior of rocks (Al-Shayea et al., 2000; Liang et al., 2017; Peng et al., 2019), and carbonate rock samples with complex pore structure show complex elastic property changes after fluid saturation, and rock samples show stronger fluid-rock skeleton interaction. As far as we know, the current research on rock at different burial depths rarely involves the influences of the micropore structure of rocks and pore water under the long-term “three high” geological environment on the mechanical response characteristics. However, the influence of the microscopic structural characteristics on the macroscopic characteristics of rocks is more significant for rocks with low porosity and permeability; moreover, rheological theory and continuum elasticity cannot reveal the microscopic mechanism of the difference between dynamic and static elastic parameters, so a comprehensive study of macroscopic mechanical parameters and microstructural parameters of rocks at different depths is helpful to deepen the understanding of the scientific phenomena of deep rocks. The extensive application of X-ray CT scanning technology provides a useful nondestructive method to obtain the microscopic structure and parameters of rock for petroleum



engineering, geotechnical mechanics and construction engineering. Based on grayscale CT or scanning electron microscopy images, digital rock technology has the advantage of being able to perform various simulations and describe the pore structure characteristics by reconstructing a digital rock model (Zhao et al., 2013; Jiang et al., 2017; Dong et al., 2018; Huaimin et al., 2018), and it is of practical significance to study the relationship between macro-mechanical behavior and micro-structure of rock (Zhang et al., 2019).

According to the above points, deep carbonate rock, which is often accompanied by low porosity and permeability, developed microstructure and significant nonlinear mechanical phenomena, could be used as a reference research object. Deep carbonate reservoirs are widely distributed around the world and account for 35% of proven deep recoverable reserves. Therefore, in this paper, the mechanical parameters of five sets of carbonate rock sampled from 6023 m to 6738 m underground in the Tarim Basin were measured under quasi *in situ* conditions. The experimental method and procedures are introduced in **Section 2**. Using high-resolution CT, five digital rocks of different depths were reconstructed, and then combined with the burial depth, their microstructural parameters and mechanical behaviors were recorded experimentally and analyzed in **Section 3**. Finally, conclusions were obtained and summarized based on this study.

2 EXPERIMENTAL METHOD AND PROCEDURES

2.1 Specimen Preparation

The full diameter carbonate core samples in experimentation were collected from the two adjacent ultra deep wells of Gucheng area of the Tarim Basin, Xinjiang Oil Field (as shown in **Figure 2**), where gathered 70 percent of ultradeep wells and 90 percent of special ultradeep wells of China. Samples with basically the same composition were divided into five groups based on their burial depth, respectively, 6077, 6234, 6488, 6652 and 6738 m

underground, and because the high coring failure rate, there were merely four to six samples per group. According to the standards specified by International Society for Rock Mechanics, the rock cores were processed into cylinders with a 50 mm dimensions of in diameter and 100 mm in height, the roughness of two end surface of the rock was confined into 0.05 mm, and the deviation of diameter was not exceed 0.5 mm. Then, to avoid the influence of oil and inorganic salt in the primary water on parameters, the samples were washed in the core automatic oil washing instrument with the organic solvent extraction method.

2.2 Experimental Setup

As shown in **Figure 3**, the experimental section was mainly composed of three parts: a triaxial compression experiment, acoustic emission velocity test and X-ray computed tomography (CT) scanning. An RTR-2000 high pressure rock triaxial dynamic testing system produced by GCTS was used for the triaxial load part to obtain the peak strength, long term strength, static elasticity modulus, static Poisson's ratio and Biot coefficient. This system can measure rock physical parameters under high temperature and pressure, and its maximum capacity of confining pressure and temperature can reach 210 MPa and 200°C, respectively, which generally conforms to the conditions tested *in situ* at a depth of 6,000 m. At the same time that the triaxial test was carried out, the dynamic elasticity modulus, dynamic Poisson's ratio, and velocity of transverse and longitudinal waves were detected by a ULT-100 ultrasonic testing instrument produced by GCTS. The instrument was equipped with a corresponding 1 MHz ultrasonic transmission and digital acquisition function to achieve the whole acoustic test process. Finally, the grayscale images of rock samples used to extract the microscopic parameters and numerical simulation were obtained from a micronanometer three-dimensional topological imaging microscopy system (MicroXCT-400, Xradia, United States). In addition, the normal triaxial confining pressure ($\sigma_1 > \sigma_2 = \sigma_3$) was adopted in this experiment.

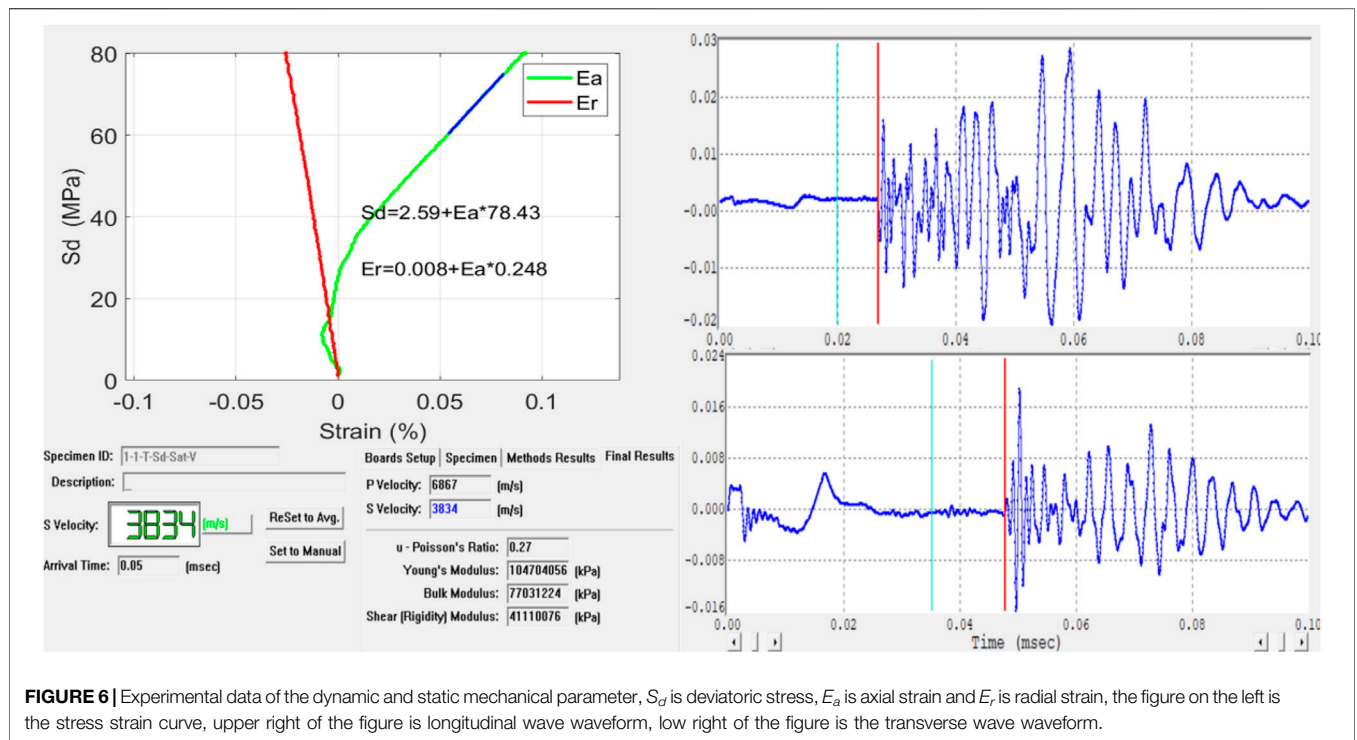


FIGURE 6 | Experimental data of the dynamic and static mechanical parameter, S_d is deviatoric stress, E_a is axial strain and E_r is radial strain, the figure on the left is the stress strain curve, upper right of the figure is longitudinal wave waveform, low right of the figure is the transverse wave waveform.

2.3 Experimental Procedures

Before carrying out the triaxial test, all of the samples were measured for basic physical properties, including the mass and density of the rock specimen, porosity, and permeability, with a

vernier caliper, electronic balance and nitrogen porosity meter. Among them, five samples were selected from different burial depths H_{dep} for full-field CT scanning at a 12 micron resolution. The CT scanning images of the samples are shown in **Figure 4**.

TABLE 1 | Experiment results and microstructure parameters of the samples for different burial depths.

SAMPLES	6077m	6234m	6488m	6652m	6738m
Porosity(%)	2.15	1.98	2.25	3.97	3.26
Density(g/cm ³)	2.8	2.81	2.72	2.68	2.64
E_p^d (GPa)	96.16	100.7	99.11	97	104.9
E_s^d (GPa)	32.83	53.64	56.33	68.93	57.66
E_p^s (GPa)	98.99	100.17	97.67	94.31	101.09
E_s^s (GPa)	60.68	60.26	49.2	32.94	72.62
μ_p^d	0.3	0.29	0.31	0.28	0.3
μ_s^d	0.203	0.204	0.225	0.222	0.208
μ_p^s	0.29	0.3	0.3	0.31	0.28
μ_s^s	0.303	0.204	0.169	0.159	0.25
σ_p (MPa)	484.1	612.8	257.6	365.8	397.4
σ_r (MPa)	369.3	469.7	201.2	308.9	364.5
σ_B (MPa)	481.2	603.86	253.94	345	392.87
B	0.156	0.199	0.422	0.261	0.098
V_p^s (m/s)	6779	6918	6824	6802	6815
V_s^s (m/s)	3702	3710	3643	3594	3753
V_p^d (m/s)	6892	6889	6814	6693	6980
V_s^d (m/s)	3783	3725	3698	3690	3808
R_p (μ m)	51.11	26.91	16.39	101.88	100.53
R_t (μ m)	42.62	19.23	8.37	52.71	64.43
L_t (μ m)	67.75	33.48	45.49	41.11	85.18
G_p	0.0299	0.0316	0.0293	0.0315	0.0317
G_t	0.0316	0.0311	0.0312	0.0318	0.0316
P_{p-t}	3.498	2.822	3.311	5.143	2.883
C	2.964	0.628	3.799	2.203	2.204

To further elucidate the mechanical properties of carbonate rock in ultradeep reservoirs, the experiment was carried out under quasi *in situ* conditions. *In situ* geology generally includes the *in situ* temperature, humidity, composition, stress, osmotic pressure, and other geological parameters (Xie et al., 2021). In this paper, we mainly consider the stress and temperature that most obviously affect the mechanical response. Temperature gradients typically range from 20°C/km to 30°C/km as the crust deepens, and this value in western and central China is approximately 25°C/km (Pang et al., 2015). According to the *in situ* stress measurement of the target area, the overburden pressure gradient is approximately 23.8 MPa/km. Thus, the ranges of the *in situ* temperature and stress of the formation in which the samples were located are approximately 150–168°C and 143–160 MPa. Different from previous studies focusing on the effect of confining pressure and temperature, this experiment aims to investigate the influence of the intrinsic properties, especially the microstructure of rocks at different burial depths, on mechanical parameters. Therefore, samples of different burial depths were tested under the same conditions of confining pressure and temperature in this work, and the specific parameter values take the value around the middle section of the target formation, i.e., the experimental temperature was 160°C, and the confining pressure was 150 MPa. Meanwhile, to study the influence of the saturation state on the transition relationship between dynamic and static mechanical parameters, samples were subjected to immersion treatment and

drying treatment in sequence to obtain the mechanical parameters in the saturated state and the dry state.

The specific experimental steps were as follows: First, the samples were put into a core vacuum saturation apparatus for 24 h, and then the saturated samples were fixed with a thermoplastic tube on the platform and sealed with a slightly heated hot fan. A pair of deformation sensors were attached to the radial and axial directions of the sample. Second, an acoustic sensor was adhered to the sample, and a coupling agent was evenly applied between the sample and the end cap of the acoustic probe to ensure sufficient coupling. Then, the experimental setup began to load the confining pressure and heat after debugging the initial sensor value. Finally, the displacement loading method was used with a loading rate of 0.002 mm/min until the axial loading pressure reached approximately 100 MPa. Considering that the peak strength of the sample is generally large, and the sample has a long elastic stage during the axial compression loading process, in order not to damage the sample as much as possible, and to ensure the accuracy of the subsequent experiments, it is not necessary to load the axial compression too much when measuring the chord modulus. Therefore, the axial pressure is added to 100 MPa when the saturated elastic modulus is measured. During the experiment, the acoustic emission signal not received by the sensor increased significantly, which proved that the microstructure of brittle carbonate samples was not damaged.

Similarly, the above process was conducted to measure the same parameters of the samples in the dry state after drying the saturated sample in a constant temperature chamber at 40°C for 24 h. However, the loading process continued until the sample broke to obtain the compressive strength and postpeak characteristics of the samples. In addition, it is worth noting that a small initial mechanical load added in this triaxial test has the ability to avoid the initial friction effect on the experimental results.

2.4 Construction of the Actual Digital Rock

Pore structure is an important factor affecting the mechanical properties and dynamic static parameter relationship of rock, especially for carbonate rocks with strong anisotropy. To describe the inner pore and fracture structures of samples from different burial depths, the actual digital rocks were constructed using a physical experimental method (Arns et al., 2004). Based on grayscale CT scanning images, we adopted the maximum classification method to generate binary images of samples after nonlocal filtering (Yu et al., 2008). Then, the rock matrix and pore–fracture space were extracted, as shown in **Figure 5**. Finally, the 3D actual digital rock was constructed by superimposing the segmented images.

According to the segmentation of pore–fracture space, the characteristics of pore structure could be quantitatively described by extracting the corresponding pore network model of samples. The model proposed that the pore network comprises pores and throats. Using the maximal ball method, the irregular cross

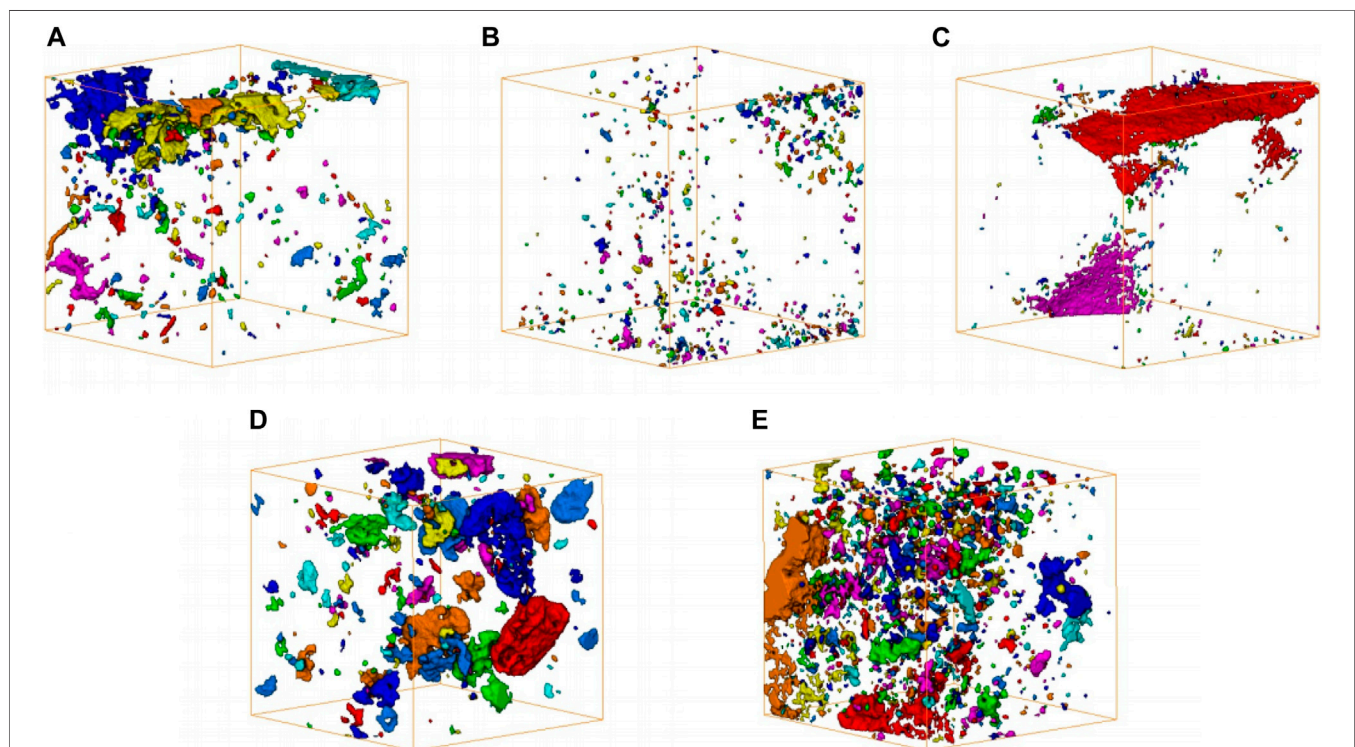


FIGURE 7 | Pore fracture space of the scanned sample at different burial depths after clustering (A) $H_{dep} = 6077$ m (B) $H_{dep} = 6234$ m (C) $H_{dep} = 6488$ m (D) $H_{dep} = 6652$ m (E) $H_{dep} = 6738$ m.

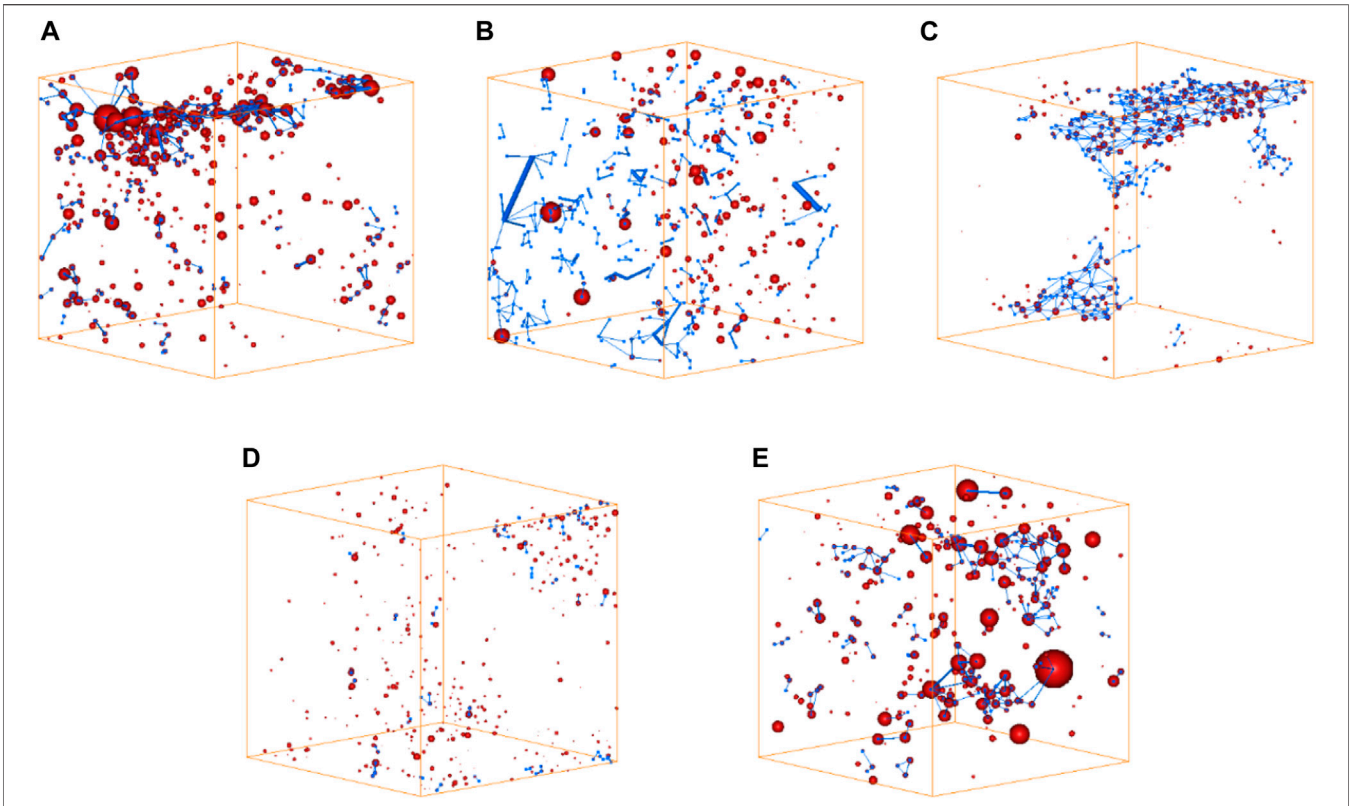


FIGURE 8 | Model pore network of the digital rock of the samples at different burial depths (A) $H_{dep} = 6077$ m (B) $H_{dep} = 6234$ m (C) $H_{dep} = 6488$ m (D) $H_{dep} = 6652$ m (E) $H_{dep} = 6738$ m.

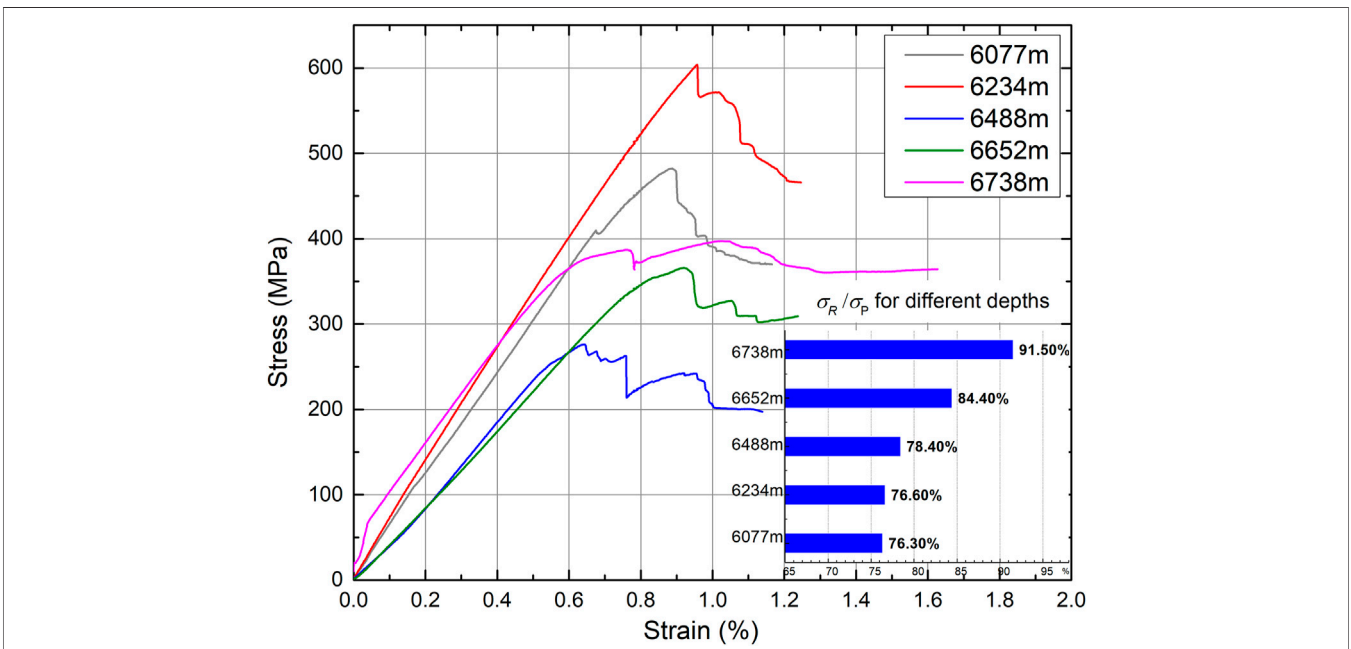
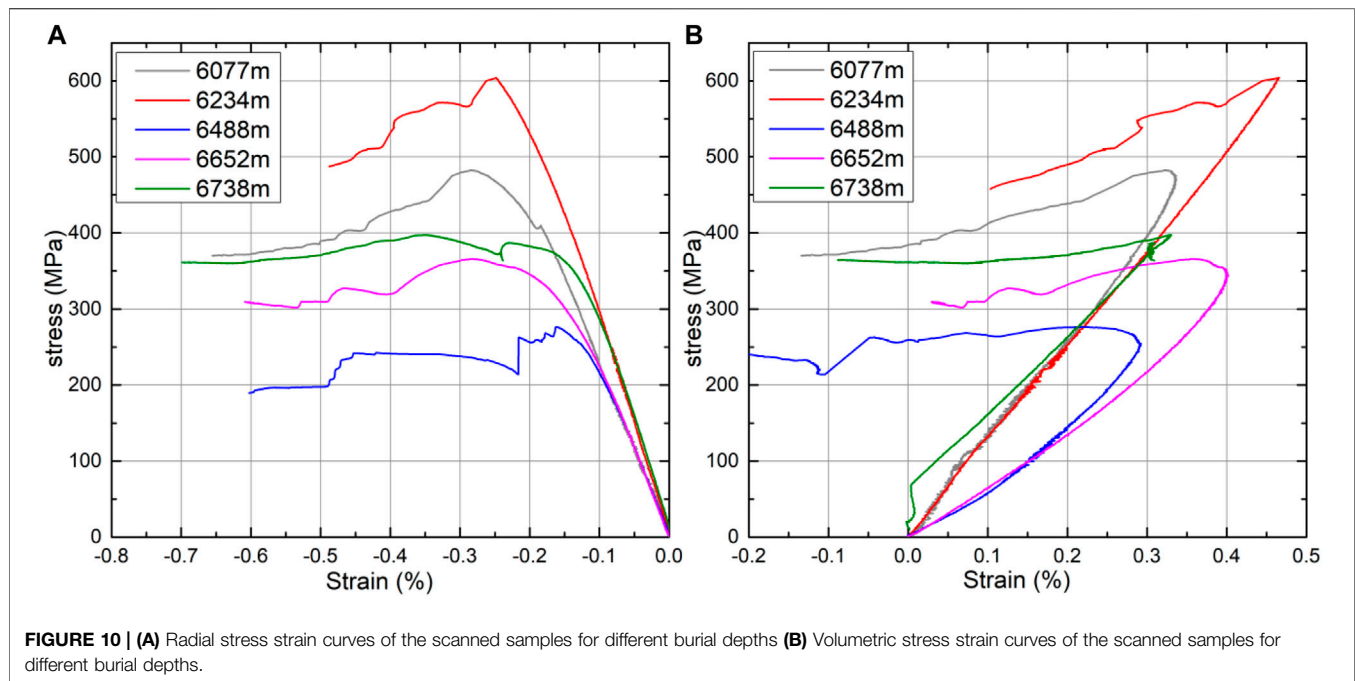


FIGURE 9 | Axial stress strain curves of the scanned samples at different burial depths.



section of pores and throats can be interpreted as different regular shapes (Pelayo and Schmidt, 2008).

The specific procedure is as follows: The isolated rock skeleton particles of the rock are removed, and then the central axis of the pore space is established by the Lee-Kashyap-Chu algorithm (Wang C.-c. et al., 2013). Then, the center position of each pore in the central axis system is determined, and the optimized pore space is optimized into pores and throats. Finally, the model of the pore network was established to reflect real pore space topology and geometric features (Wang C.-c. et al., 2013).

According to the statistical information of the pore network model extracted by using the maximal ball method, the structural parameters can be obtained, including the pore throat ratio, pore and throat radius, coordination number, and throat and pore shape factor. Among them, the nondimensional shape factor G characterizes the degrees of irregularity of pores or throats defined by:

$$G = \frac{VL}{A_s^2} \quad (1)$$

where V is the volume of the pore or throat space, L is the length of the pore or throat space, and A_s is the surface area of the pore or throat space. Therefore, the positive correlation of the value of G indicates the regularity of the pore or throat space; for instance, G reaches the maximum when the space is round, and a triangular G is in the range of 0–0.0481. In addition, the process of simplification follows the principle of shape factor conservation, i.e., the geometry used to characterize a pore or throat has a shape factor equal to the shape factor of the pore or throat.

3 EXPERIMENTAL RESULTS AND DISCUSSION

As shown in Figure 6, the chord modulus E_{ch} was chosen as the calculation method of the static elasticity modulus E_S (Spencer Jr, 1981), i.e., the slope of string between the arbitrary two point of the stress strain curve in the elastic range, and the static Poisson's ratio μ_s is given by:

$$\mu_s = |\varepsilon_{d(50)} / \varepsilon_{h(50)}| \quad (2)$$

where $\varepsilon_{d(50)}$, $\varepsilon_{h(50)}$ are the axial and radial compression strain when the principle stress difference is 50% of the maximum value. The conventional transmission was used in the wave velocity measurement, namely, calculate the wave velocity by reading the arrival time of the wave head, which can be represented by:

$$V_p = \frac{L}{T_p} = \frac{L}{T_{PM} - T_{PO}} \times 10^{-3}$$

$$V_s = \frac{L}{T_s} = \frac{L}{T_{SM} - T_{SO}} \times 10^{-3} \quad (3)$$

where L is the length of sample (mm), V_s and V_p are the transverse and longitudinal wave velocity, T_s and T_p are the propagation time of the transverse and longitudinal wave in samples (μ s), T_{SM} and T_{PM} are the instrument reading during the transverse and longitudinal measurements (μ s), and T_{SO} , T_{PO} are the zero reading of the instrument (μ s).

Then, the dynamic elasticity modulus E_D and the dynamic Poisson's ratio μ_D respectively defined by:

$$E_D = \frac{\rho V_s^2 (3V_p^2 - 4V_s^2)}{V_p^2 - V_s^2}$$

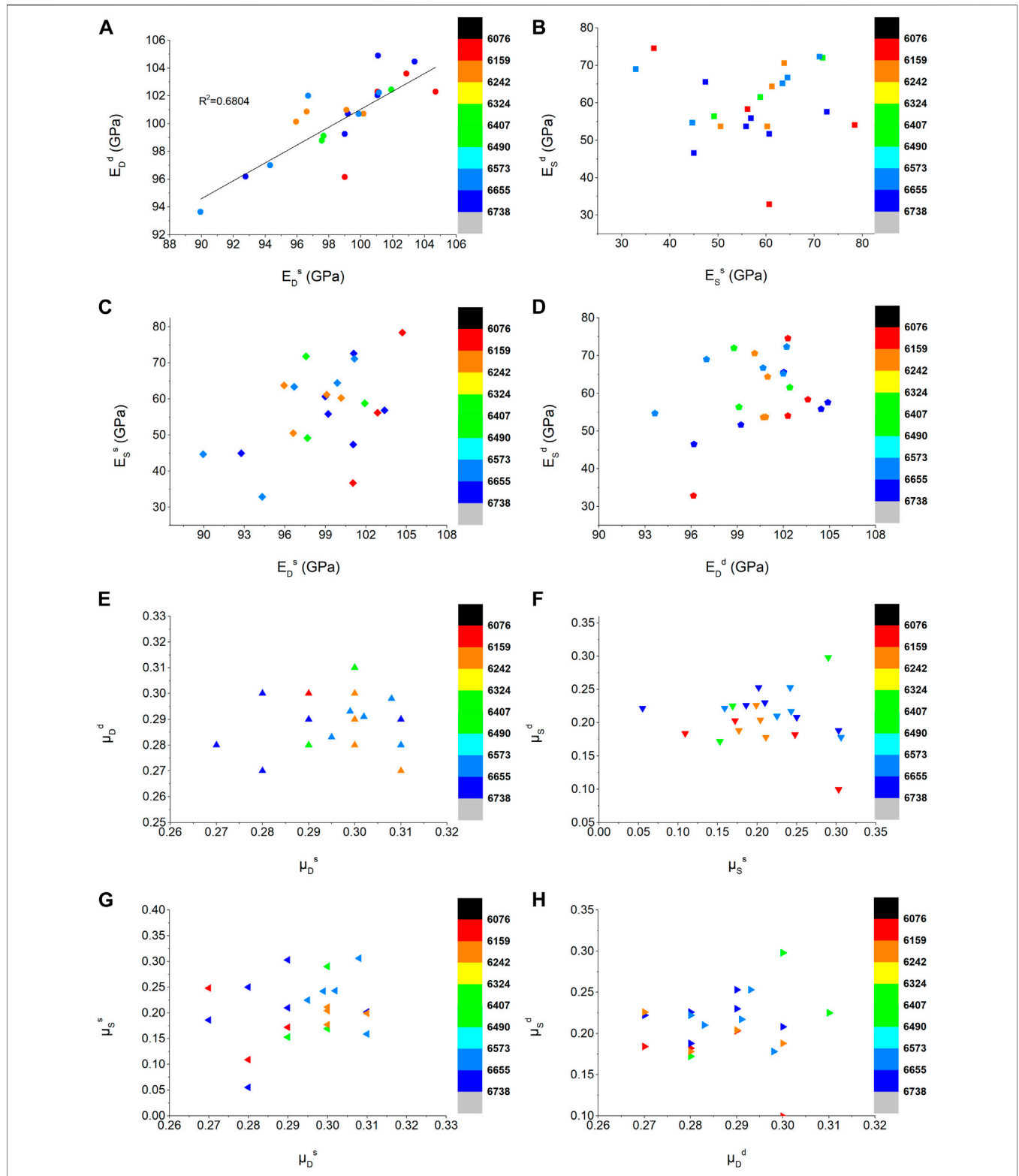


FIGURE 11 | (A) Relationship of E_D^d and E_D^s of all samples at different burial depths (B) Relationship of E_S^d and E_S^s at different burial depths (C) Relationship of E_S^s and E_D^s at different burial depths (D) Relationship of E_S^d and E_D^d at different burial depths (E) Relationship of μ_D^d and μ_D^s at different burial depths (F) Relationship of μ_S^d and μ_S^s at different burial depths (G) Relationship of μ_S^s and μ_D^s at different burial depths (H) Relationship of μ_S^d and μ_D^d at different burial depths.

$$\mu_D = \frac{V_p^2 - 2V_s^2}{2(V_p^2 - V_s^2)} \quad (4)$$

and we set the elasticity modulus in saturated and dry states as E^s and E^d . Finally, the experiment results and the microstructure parameters of the samples for different burial depths were summarized in **Table 1**, where σ_P is the peak strength, σ_R is the residual strength and σ_B is the long term strength, B is the Biot coefficient, R_p is the mean pore radius, R_t is the mean throat radius, L_t is the mean throat length, G_p is the mean pore shape factor, G_t is the mean throat shape factor, P_{p-t} is the mean pore throat ratio and C is the coordination number. In addition, the pore fracture space of the samples for different burial depths after clustering were presented in **Figure 7**, the model pore network of digital rock for different burial depths were presented in **Figure 8**.

3.1 Stress Strain Characteristics of the Cores From Different Burial Depths

The stress-strain curves of the samples chosen for CT scanning obtained under triaxial compression are displayed in **Figures 9, 10**. Clearly, there is a large span between the peak strength of different burial depths; the minimum peak strength of the five sets of rock samples is 262.5 MPa, and the maximum peak reaches 612.8 MPa. The results reflect the strong heterogeneity of the carbonate reservoir, which does not show a significant correlation with burial depth.

Remarkably, samples of different burial depths present discrepant postpeak characteristics, all of which exhibit plastic flow, especially for a sample burial depth of 6738 m, but the samples buried at 6488, 6652 and 6738 m alternately exhibit strain hardening and strain softening; this seems to be more pronounced in samples of low strength. In **Figure 7C-E**, this phenomenon could be construed as

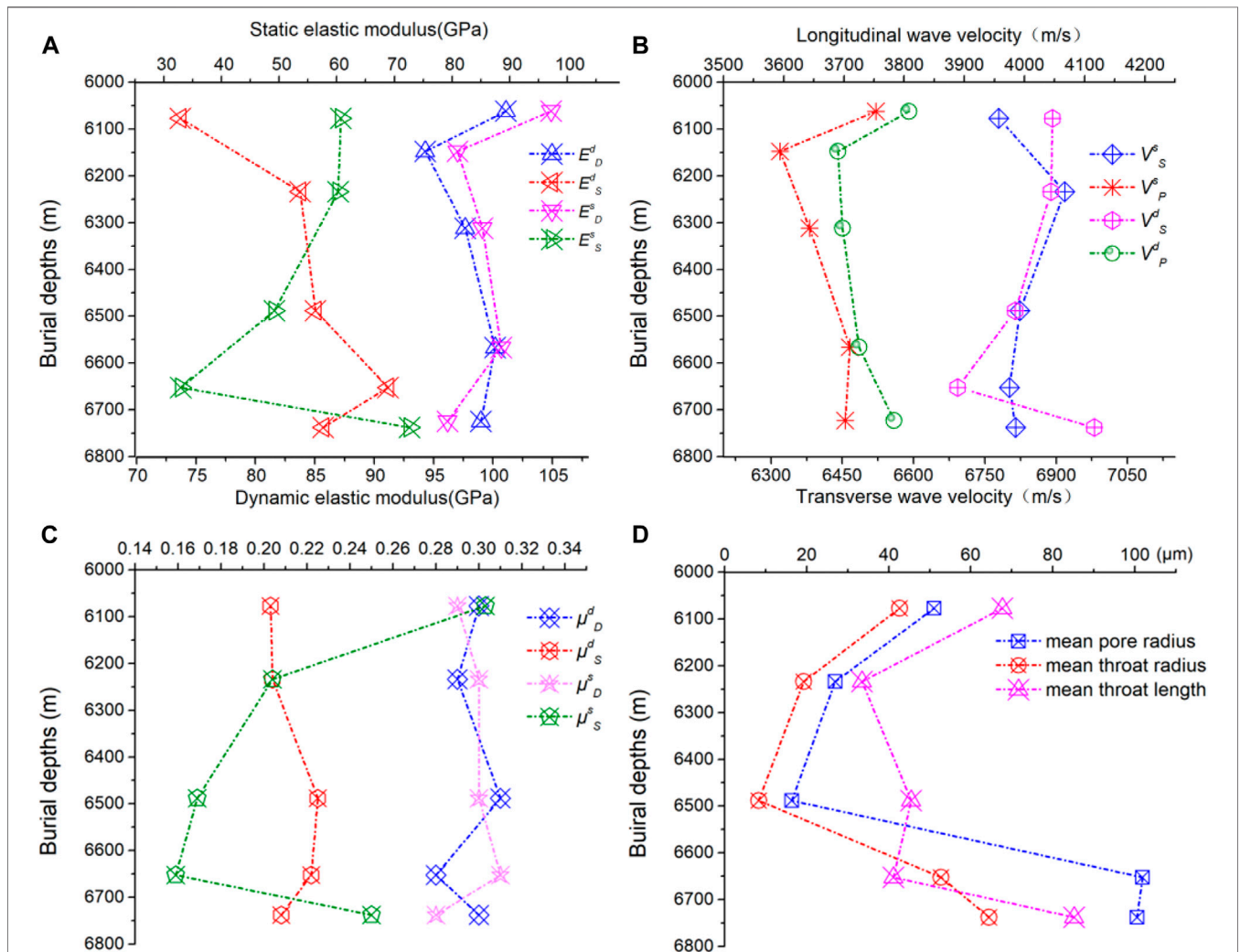
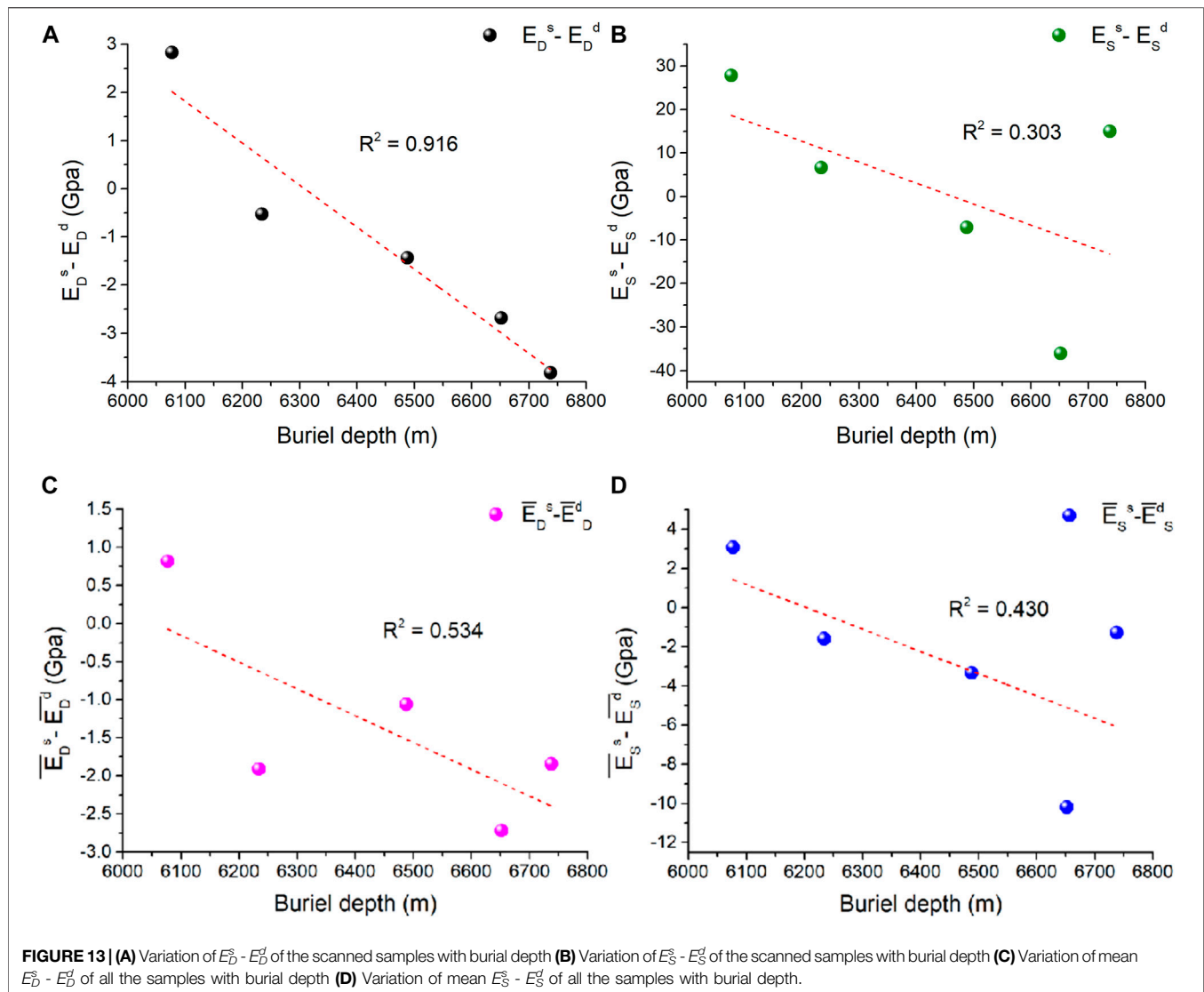


FIGURE 12 | (A) E_D^d , E_S^d , E_D^s and E_S^s of the scanned samples at different burial depths (B) V_S^d , V_P^d , V_S^s and V_P^s of the scanned samples at different burial depths (C) μ_D^d , μ_S^d and μ_S^s of the scanned samples at different burial depths (D) mean R_p , R_t and L_t of the scanned samples at different burial depths.

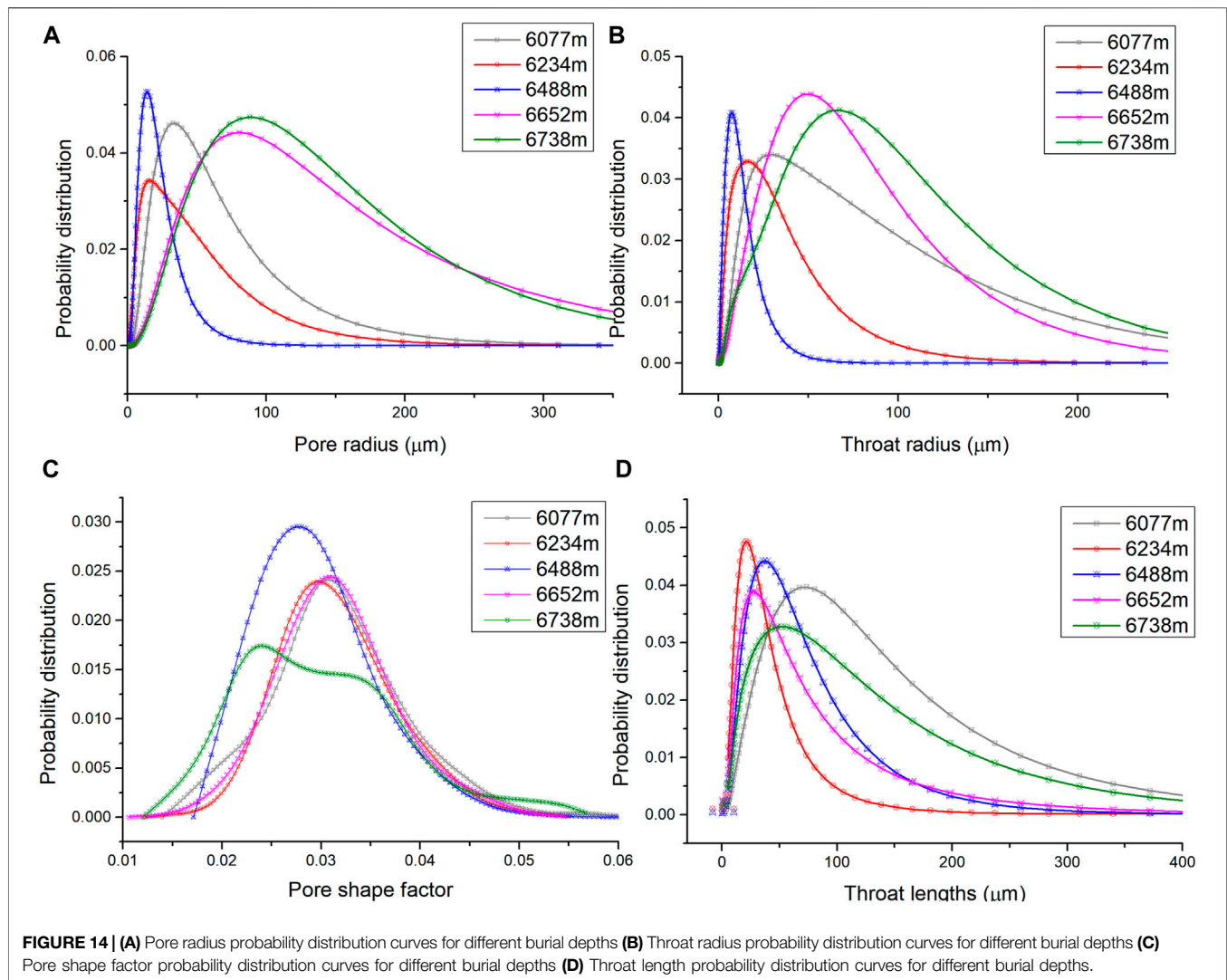


samples with weaker structures (fractures and caves, **Figure 7C–E**) becoming more prone to local instability after compaction and developing microfractures; after the strain softening process during the recompaction of expanded microfractures, the sample has increased strength manifested as strain hardening, and the effect of fracture on rock strength is more obvious.

In **Figure 9**, we can see that the samples have both high levels of peak strength and residual strength. After the process of compression achieves the ultimate failure stress, the nonlinear rebound of the stress–strain curves is more evident as the burial depth increases. It is worth noting that the residual strength is closer to its corresponding peak strength as the burial depth increases, and the ratios of residual strength to peak strength in sequence are 76.3%, 76.6%, 78.4%, 84.4%, 91.5% as the burial depth increases. This may be due to the pore structure, the method and degree of cementation and other factors of the more deeply buried samples under the long-term “three high” geological environment that make the sample exhibit more plasticity under high stress. Although the influence of

temperature on the dislocation motion of the carbonate is not significant (Araújo et al., 1997), the influence of pressure on mechanical twin crystals, such as calcite in carbonate, is obvious.

As shown in **Figure 10A**, the radial strain obviously lags behind the axial strain, and the peak of the radial stress–strain curves are more rounded compared with the axial stress–strain curves, which may indicate that the radial samples have a stronger resistance to damage. As shown in **Figure 10B**, the samples buried at 6234 m, 6488 m and 6738 m exhibit rock dilatancy (Cook, 1970). Alkan et al. (2007) defined the turning point of the volume from compression to expansion as the compression–expansion boundary (C/D boundary), and Martin (Martin and Read, 1992) considered that the axial stress corresponding to the C/D boundary is the crack damage stress, namely, the long-term strength σ_B . In general, the long-term strength is between 60% and 80% of the peak strength (Szczechpanik et al., 2003); however, the long-term strength reaches 94%–99% of the peak strength in this experiment (as shown in **Table 1**). This is also the result of the rock being under high *in situ* stress for a long time.



3.2 Elastic modulus and Poisson' ratio of the cores from different burial depths

The dynamic and static mechanical parameters and the conversion relationship between them play an important guiding role in underground engineering and the process of oil and gas development. Compared with sandstone, limestone or mudstone, carbonate rocks have a poorer dynamic and static correlation, and the accuracy of the dynamic–static parameter conversion model often decreases with increasing burial depth. The main factors causing the difference of dynamic and static elastic moduli are the effect of pore structure on wave propagation, the occurrence state of fluid and the velocity dispersion (Warpinski et al., 1998), Jing et al.(2016; 2017) has done meaningful work on the analysis and understanding of strong compressional wave velocity dispersion and the influence of fabric and saturation inhomogeneity on wave propagation by establishing theoretical models. And the relationship between the static and dynamic mechanical parameters of all samples in the dry or saturated state is displayed in **Figure 11**.

As shown in **Figures 11A,B**, there is a certain linear relationship between E_D^d and E_D^s ; however, E_S^d and E_S^s are not the case, and compared to the dynamic modulus, the presence of pore water has a more obvious impact on the static mechanical parameters (**Figure 12A, C**). In general, for rocks that are not prone to physicochemical reactions with water, the presence of incompressible pore water has an effect of resistance on longitudinal deformation of the sample during loading, which is reflected in the macromechanical parameter being the increase in elastic modulus. However, in this experiment, the influence of pore water on the elastic modulus may be increased or decreased. By analyzing the relationship between the $E^s - E^d$ of the samples and their burial depth, **Figure 13** illustrates that the effect of pore water on the elastic modulus is related to the burial depth of the sample. At a relatively shallow position, pore water increases the elastic modulus, but with increasing depth, the influence of pore water on the elastic modulus tends to decrease. Combining the conclusions from the previous section that pore structure, the method and degree of cementation and other factors of the buried deeper samples under the long-term “three high” geological environment make the sample

exhibit more plasticity with increased burial depth, the results in **Figure 13** can be interpreted as the deeper-buried samples under high stress for a long time exhibit more plasticity, and their dynamic and static elastic modulus is more likely to be weakened by pore water. This phenomenon seems to be more pronounced for the dynamic modulus than for the static modulus. In addition, the mean values of $E^s - E^d$ of all samples show a similar trend with the $E^s - E^d$ of five samples for the CT scan (**Figure 13A,C**, **Figure 13B,D**), which reflects the representativeness of the sample selected for scanning to some extent.

The main internal factors that cause the difference in dynamic and static mechanical parameters are pore structure, fracture and pore fluid. As shown in **Figure 11C** and **Figure 12D**, the correlation between E_D and E_S is poor regardless of the presence of pore fluid for different burial depths. On the other hand, the difference in dynamic parameters between samples is smaller than that in static parameters, the maximum values of E_D^d and E_D^s are 104.91 and 104.70 GPa, and the minimum values of E_D^d and E_D^s are 93.65 and 89.94 GPa. Correspondingly, the maximum values of E_S^d and E_S^s are 74.56 and 78.43 GPa, and the minimum values of E_S^d and E_S^s are 32.83 and 32.94 GPa. The ratio of E_S to E_D is approximately 0.4–0.7, and the average values of E_S^d/E_D^d and E_S^s/E_D^s are 0.592 and 0.578, respectively. This is approximate to the Evans. (1973) and Warpinski et al. (1998) view that the static elastic modulus is one half of its dynamic elastic modulus.

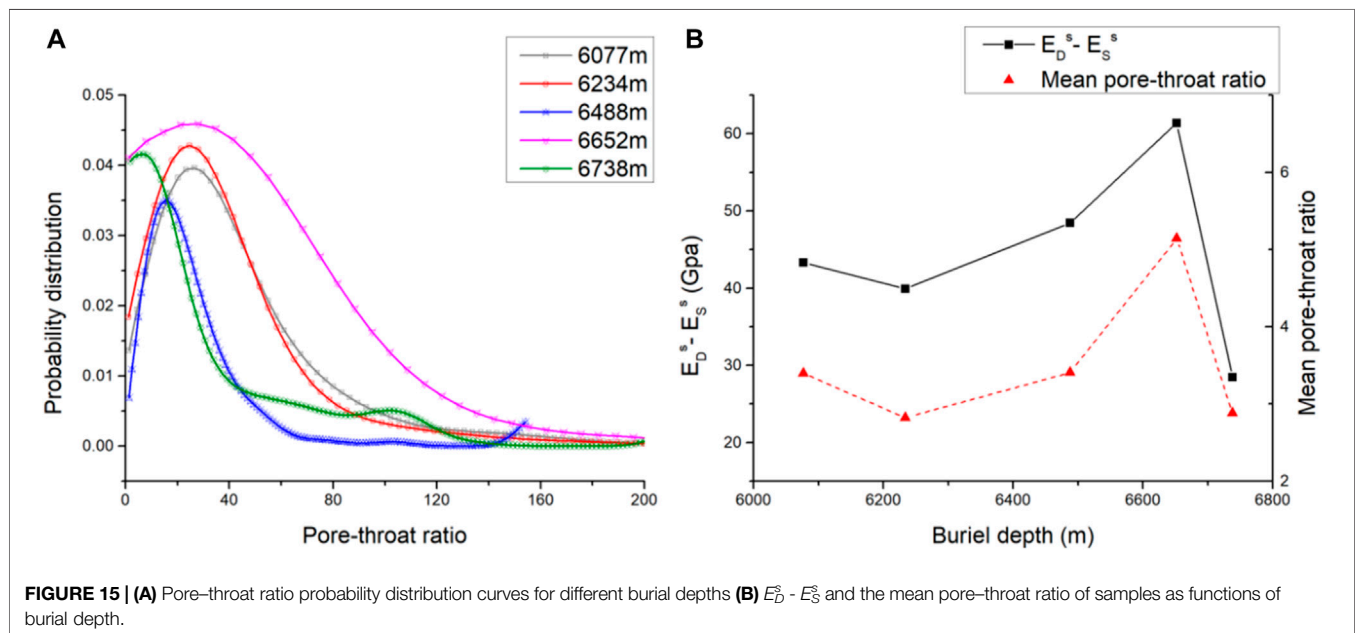
3.3 Structural Parameters of the Pore Network Model From Different Burial Depths

A schematic of the parameters of the pore structure probability distribution from different burial depths is shown in **Figures 14, 15**, and the pore size variation with burial depth is presented in

Figure 12D. The probability distribution of these structural parameters reflects the geometric properties of the samples and attempts to display the effect of depth change on the geometric size and shape of the pore and throat in the pore network model. **Figure 13D** shows that the pore-throat size of the sample decreases first and then increases with increasing depth. As shown in **Figure 14A** and **Figure 14B**, the pore radius and throat radius of the samples are situated on the same order of magnitude, reflecting that the samples have small pores and thin throats in porous media. The distributions of pore and throat radii differ widely among the samples and have a complex pore size structure. The pore and throat degree of sorting, which represents the concentration of the size distribution, first decreases and then increases with burial depth, and it is positively related to pore throat size. The pore throat degrees of sorting of samples at 6652 m and 6738 m are smaller than those of the shallower rocks; moreover, the pore throat degree of sorting of samples at 6488 m is maximal, and the peaks are focused at approximately 20 and 12 μm .

In **Figure 14C**, we can see that, except for the 6738 m sample, the pore shape factors of other samples have normal distribution characteristics, of which the probability distributions of the burial depths at 6077, 6234 and 6652 m are similar and their pore shape factors are mainly approximately 0.03. In contrast, the probability distributions of the 6738 m sample have three peaks near 0.022, 0.034 and 0.054, which indicates that the samples have more abundant cave and fracture structures. The probability distribution of throat lengths displayed in **Figure 14D** presents a contradistinctive result to the probability distribution of pore and throat radius, the samples of 6077 and 6738 m have a longer throat compared to the other samples, and even those above 300 μm are still distributed.

The pore-throat ratio, which refers to the ratio of the pores in the local range to the average of the radius of all the throat connections,



is regarded as a commonly used parameter to evaluate the homogeneity of the pore network model. Specifically, the decrease in the pore throat ratio is embodied in the decrease between the pore radius and throat radius, namely, the more uniform the development of the pore space on the microscopic scale. The probability distribution of the pore–throat ratio for different burial depths is displayed in **Figure 15A**.

As shown in the plot of $E_D^s - E_S^s$ and the mean pore–throat ratio of samples as a function of burial depth in **Figure 15B**, it is obvious that limited by the strong heterogeneity of the reservoir and the number of samples, although $E_D^s - E_S^s$ does not present an apparent regularity of variation with burial depth, the values of $E_D^s - E_S^s$ are significantly connected with the mean pore–throat ratios. $E_D^s - E_S^s$, as a function of the mean pore–throat ratio R_{p-t} , can be expressed as:

$$E_D^s - E_S^s = 11.396R_{p-t} + 4.0726 (R^2 = 0.7966) \quad (5)$$

The pore–throat ratio has always been regarded as an important microstructural parameter that affects the permeability and electrical properties of rocks; however, this result indicates that the pore–throat structure form has an influence on the difference in dynamic and static elastic modulus in the presence of pore water.

4 CONCLUSION

This study attempts to study the microstructure and macromechanical behavior of carbonate rocks obtained from five different burial depths (6077–6738 m underground). To focus on the intrinsic properties of rocks at different burial depths, five groups of samples from different depths were subjected to triaxial testing under a confining pressure and temperature of approximately 6,400 m (150 MPa, 160°C), and the microstructural parameters of five samples from different groups were extracted by CT scanning and digital rock modeling. The following conclusions can be drawn:

- (1) Due to the strong anisotropism and the inherent limits of the number of samples, the peak strength, residual strength, wave velocity, and static and dynamic elastic modulus of the samples do not show obvious correlations with burial depth, and the same is true for the microstructural parameters. However, the microstructure of the samples has a significant influence on the macroscopic mechanical behaviors.
- (2) Different from the long-term strength of shallow rock, which is 60%–80% of the peak strength, the long-term strength of the samples in this experiment can reach 94%–99% of the peak strength. This reflects the influence of long-term high stress on the rock strength structure.
- (3) With increasing depth, the plastic characteristics of the samples become more obvious, and the ratios of the residual strength to its peak strength increase with increasing burial depth, which in sequence are 76.3%, 76.6%, 78.4%, 84.4%, and 91.5%. The samples with more developed fractures and caves alternately experience strain hardening and strain softening during the postpeak stage. This phenomenon may be explained by the fact that samples with more weak structures are more prone to local instability

after compaction and develop microfractures. After the strain softening process during the recompaction of expanded microfractures, the sample has stronger strength manifested as strain hardening.

- (4) The influence of pore water on the elastic modulus of samples varies with burial depth. Within the depth of the samples in this experiment, pore water can enhance the elastic modulus of relatively shallow samples and weaken the elastic modulus of relatively deep samples. $E^s - E^d$ has a linear decreasing relationship with burial depth; this phenomenon is more obvious for the dynamic modulus.
- (5) The probability distribution of pore radius, throat radius, pore shape factor, throat length and pore–throat ratio for different burial depths are presented. The results showed that the sample had small pores and thin throats in porous media, and the pore–throat size generally decreased and then increased with increasing depth. Moreover, the values of $E_D^s - E_S^s$ are significantly connected with the mean pore–throat ratios, and $E_D^s - E_S^s$ can be expressed as a function of the mean pore–throat ratio R_{p-t} .

Conventional triaxial experiments combined with digital core technology that can analyze and observe microstructures help us better understand the macromechanical behavior of rocks. Limited by the number of samples, the experimental results only provide a certain degree of reference for deep rock mechanics. But through this work, we can clearly see that deep rock under the three-high environment for a long time exhibits some characteristics that differ from shallow rocks, while some features have a certain relationship with the buried depth. This further shows that targeted experiments and theoretical research on deep rock are necessary.

DATA AVAILABILITY STATEMENT

The original contributions presented in the study are included in the article/Supplementary Material, further inquiries can be directed to the corresponding author.

AUTHOR CONTRIBUTIONS

JS and ZC contributed to conception of the study, RZ wrote the first draft of the manuscript, HC was in charge of the experiments in the rock mechanics section, BX performed the statistical analysis and the modeling of digital rocks, RZ, JS, ZC and BX wrote sections of the manuscript. All authors contributed to manuscript revision, read, and approved the submitted version.

FUNDING

This work was financially supported by the National Natural Science Foundation of China (Grants No. 41874138), Innovative Project for Graduate Students (Grant Nos. YCX2021024).

REFERENCES

- Al-Shayea, N. A., Khan, K., and Abduljawwad, S. N. (2000). Effects of Confining Pressure and Temperature on Mixed-Mode (I-II) Fracture Toughness of a limestone Rock. *Int. J. Rock Mech. Mining Sci.* 37 (4), 629–643. doi:10.1016/s1365-1609(00)00003-4
- Alkan, H., Cinar, Y., and Pusch, G. (2007). Rock Salt Dilatancy Boundary from Combined Acoustic Emission and Triaxial Compression Tests. *Int. J. Rock Mech. Mining Sci.* 44 (1), 108–119. doi:10.1016/j.ijrmms.2006.05.003
- Araújo, R., Sousa, J., and Bloch, M. (1997). Experimental Investigation on the Influence of Temperature on the Mechanical Properties of Reservoir Rocks. *Int. J. Rock Mech. Mining Sci.* 34 (3-4), 298–e291298. e216. doi:10.1016/s1365-1609(97)00065-8
- Arns, C. H., Knackstedt, M. A., Pinczewski, W. V., and Martys, N. S. (2004). Virtual Permeametry on Microtomographic Images. *J. Pet. Sci. Eng.* 45 (1-2), 41–46. doi:10.1016/j.petrol.2004.05.001
- Avseth, P., Flesche, H., and Van Wijngaarden, A.-J. (2003). AVO Classification of Lithology and Pore Fluids Constrained by Rock Physics Depth Trends. *The Leading Edge* 22 (10), 1004–1011. doi:10.1190/1.1623641
- Cook, N. G. W. (1970). An experiment Proving that Dilatancy Is a Pervasive Volumetric Property of Brittle Rock Loaded to Failure. *Rock Mech.* 2 (4), 181–188. doi:10.1007/bf01245573
- De Santis, F., Renaud, V., Gunzburger, Y., Kinscher, J., Bernard, P., and Contrucci, I. (2020). *In Situ* monitoring and 3D Geomechanical Numerical Modelling to Evaluate Seismic and Aseismic Rock Deformation in Response to Deep Mining. *Int. J. Rock Mech. Mining Sci.* 129, 104273. doi:10.1016/j.ijrmms.2020.104273
- Dong, H., Sun, J., Lin, Z., Fang, H., Li, Y., Cui, L., et al. (2018). 3D Pore-type Digital Rock Modeling of Natural Gas Hydrate for Permafrost and Numerical Simulation of Electrical Properties. *J. Geophys. Eng.* 15 (1), 275–285. doi:10.1088/1742-2140/aa8a8e
- Dyman, T. S., Schmoker, J. W., and Root, D. H. (1998). USGS Assesses Deep Undiscovered Gas Resource. *Oil Gas J.* 96, 16.
- Evans, W. M. (1973). *A System for Combined Determination of Dynamic and Static Elastic Properties, Permeability, Porosity and Resistivity of Rocks*. Austin, TX: The University of Texas at Austin.
- Gong, F., Ye, H., and Luo, Y. (2018). The Effect of High Loading Rate on the Behaviour and Mechanical Properties of Coal-Rock Combined Body. *Shock and vibration*, 1–9. doi:10.1155/2018/4374530
- Hoek, E., and Brown, E. (1997). Practical Estimates of Rock Mass Strength. *Int. J. Rock Mech. Mining Sci.* 34 (8), 1165–171. doi:10.1016/s1365-1609(97)80069-x
- Huaimin, D., Jianmeng, S., Likai, C., Liyuan, S., Weichao, Y., Yafen, L., et al. (2018). Study on the Effects of Natural Gas Hydrate Cementation Mode on the Physical Properties of Rocks. *J. Geophys. Eng.* 15 (4), 1399–1406. doi:10.1088/1742-2140/aab625
- Huang, X., Pang, J., Liu, G., and Chen, Y. (2020). Experimental Study on Physicomechanical Properties of Deep sandstone by Coupling of Dry-Wet Cycles and Acidic Environment. *Adv. Civil Eng* 4, 1–17. doi:10.1155/2020/2760952
- Jiang, Y., Sun, J., Gao, J., Zhang, P., and Cui, J. (2017). A Simulation of Mud Invasion and Characteristics of Array Laterolog Responses in a Low-Permeability Gas Reservoir: a Case Study. *J. Geophys. Eng.* 14 (3), 456–465. doi:10.1088/1742-2140/aa5e69
- Jing, B., Xu, W., Fu, L., Carcione, J. M., and Lin, Z. (2017). Rock Anelasticity Due to Patchy Saturation and Fabric Heterogeneity: A Double Double-porosity Model of Wave Propagation. *J. Geophys. Res. Solid Earth* 122, S1. doi:10.1002/2017jb014667
- Jing, H., Xingxing, C., Jose, M., and Haung, X. (2016). Compressional Wave Dispersion Due to Rock Matrix Stiffening by clay Squeezing Flow. *Geophys. Res. Lett.* 43 (12), 6186–6195. doi:10.1002/2016GL069312
- Kaiser, P. K., and Cai, M. (2012). Design of Rock Support System under Rockburst Condition. *J. Rock Mech. Geotechnical Eng.* 4 (3), 215–227. doi:10.3724/sp.j.1235.2012.00215
- Kaiser, P. K., and Kim, B.-H. (2015). Characterization of Strength of Intact Brittle Rock Considering Confinement-dependent Failure Processes. *Rock Mech. Rock Eng.* 48 (1), 107–119. doi:10.1007/s00603-014-0545-5
- Kang, K.-J., Cheng, J.-P., Chen, Y.-H., Li, Y., Shen, M., Wu, S., et al. (2010). “Status and Prospects of a Deep Underground Laboratory in China,” in Proceedings, 11th International Conference on Topics in astroparticle and underground physics in Memory of Julio Morales (TAUP 2009), Rome, Italy, July 1-5, 2009 (Rome, Italy: IOP Publishing), 012028.
- Kang, P., Zhaopeng, L., Quanle, Z., Zhenyu, Z., and Jiaqi, Z. (2019). Static and Dynamic Mechanical Properties of Granite from Various Burial Depths. *Rock Mech. Rock Eng.* 52 (10), 3545–3566. doi:10.1007/s00603-019-01810-y
- Li, C., Xie, H., and Wang, J. (2020). Anisotropic Characteristics of Crack Initiation and Crack Damage Thresholds for Shale. *Int. J. Rock Mech. Mining Sci.* 126, 104178. doi:10.1016/j.ijrmms.2019.104178
- Li, S. C., Feng, X. D., and Li, S. C. (2013). Numerical Model for the Zonal Disintegration of the Rock Mass Around Deep Underground Workings. *Theor. Appl. Fracture Mech.* 67–68, 65–73. doi:10.1016/j.tafmec.2013.11.005
- Liang, Y., Li, Q., Gu, Y., and Zou, Q. (2017). Mechanical and Acoustic Emission Characteristics of Rock: Effect of Loading and Unloading Confining Pressure at the Postpeak Stage. *J. Nat. Gas Sci. Eng.* 44, 54–64. doi:10.1016/j.jngse.2017.04.012
- Liang, Z., Chen, Z., and Rahman, S. S. (2020). Experimental Investigation of the Primary and Secondary Creep Behaviour of Shale Gas Reservoir Rocks from Deep Sections of the Cooper Basin. *J. Nat. Gas Sci. Eng.* 73, 103044. doi:10.1016/j.jngse.2019.103044
- Malan, D., and Basson, F. (1998). Ultra-deep Mining: the Increased Potential for Squeezing Conditions. *J. South. Afr. Inst. Mining Metall.* 98 (7), 353–363.
- Malan, D. F. (1999). Time-dependent Behaviour of Deep Level Tabular Excavations in Hard Rock. *Rock Mech. Rock Eng.* 32 (2), 123–155. doi:10.1007/s006030050028
- Martin, C., and Derek, C. (1993). The Strength of Massive Lac du Bonnet Granite Around Underground Openings [microform]. Dissertation Abstracts International.
- Pang, X.-Q., Jia, C.-Z., and Wang, W.-Y. (2015). Petroleum Geology Features and Research Developments of Hydrocarbon Accumulation in Deep Petroliferous Basins. *Pet. Sci.* 12 (1), 1–53. doi:10.1007/s12182-015-0014-0
- Pelayo, A., and Schmidt, B. (2008). Maximal ball Packings of Symplectic-Toric Manifolds. *Int. Math. Res. Notices*, 121–136. doi:10.48550/arXiv.0704.1036
- Peng, K., Liu, Z., Zou, Q., Wu, Q., and Zhou, J. (2020). Mechanical Property of Granite from Different Buried Depths under Uniaxial Compression and Dynamic Impact: an Energy-Based Investigation. *Powder Tech.* 362, 729–744. doi:10.1016/j.powtec.2019.11.101
- Peng, K., Zhou, J., Zou, Q., and Yan, F. (2019). Deformation Characteristics of Sandstones during Cyclic Loading and Unloading with Varying Lower Limits of Stress under Different Confining Pressures. *Int. J. Fatigue* 127, 82–100. doi:10.1016/j.ijfatigue.2019.06.007
- Pusch, R. (1993). Mechanisms and Consequences of Creep in Crystalline Rock. *Compr. rock Eng.* 1, 227–241.
- Ranjith, P. G., Zhao, J., Ju, M., De Silva, R. V. S., Rathnaweera, T. D., and Bandara, A. K. M. S. (2017). Opportunities and Challenges in Deep Mining: a Brief Review. *Engineering* 3 (4), 546–551. doi:10.1016/j.eng.2017.04.024
- Singh, J., Ramamurthy, T., and Rao, G. (1989). “Strength of Rocks at Depth,” in ISRM International Symposium, Pau, France, August 30–September 2, 1989 (Pau, France: OnePetro).
- Spencer, J. W., Jr (1981). Stress Relaxations at Low Frequencies in Fluid-Saturated Rocks: Attenuation and Modulus Dispersion. *J. Geophys. Res.* 86 (B3), 1803–1812. doi:10.1029/jb086ib03p01803
- Szczepanik, Z., Milne, D., Kostakis, K., and Eberhardt, E. (2003). “Long Term Laboratory Strength Tests in Hard Rock,” in 10th ISRM Congress: Johannesburg: OnePetro.
- Tang, C. (1997). Numerical Simulation of Progressive Rock Failure and Associated Seismicity. *Int. J. Rock Mech. Mining Sci.* 34 (2), 249–261. doi:10.1016/s0148-9062(96)00039-3
- Tarasov, B. G., and Randolph, M. F. (2008). Frictionless Shear at Great Depth and Other Paradoxes of Hard Rocks. *Int. J. Rock Mech. Mining Sci.* 45 (3), 316–328. doi:10.1016/j.ijrmms.2007.06.001
- Tzanakis, C. (1997). The Quest of beauty in Research and Teaching of Mathematics and Physics: A Historical Approach. *Nonlinear Anal. Theor. Methods Appl.* 30 (4), 2097–2105. doi:10.1016/s0362-546x(96)00249-0

- Vorobiev, O. Y., and Morris, J. P. (2019). Modeling Dynamic Fracture in Granite under *In Situ* Conditions at High Temperatures and Pressures. *Int. J. Rock Mech. Mining Sci.* 113, 241–254. doi:10.1016/j.ijrmms.2018.11.007
- Wang, C.-C., Yao, J., Yang, Y.-F., and Wang, X. (2013a). Study on Resolution Selection for Digital Rock Construction with CT Scanning Method. *Sci. Tech. Eng.* 13, 1671–1815.
- Wang, J., Feng, L., Zhao, L., and Snowden, S. (2013b). China's Natural Gas: Resources, Production and its Impacts. *Energy Policy* 55, 690–698. doi:10.1016/j.enpol.2012.12.034
- Wang, Y., Guo, P., Dai, F., Li, X., Zhao, Y., and Liu, Y. (2018). Behavior and Modeling of Fiber-Reinforced clay under Triaxial Compression by Combining the Superposition Method with the Energy-Based Homogenization Technique. *Int. J. Geomech.* 18 (12), 04018172. doi:10.1061/(asce)gm.1943-5622.0001313
- Warpinski, N., Peterson, R., Branagan, P., Engler, B., and Wollhart, S. (1998). "In Situ stress and Moduli: Comparison of Values Derived from Multiple Techniques," in SPE annual technical conference and exhibition, New Orleans, LA, September 27–30, 1998 (New Orleans, LA: OnePetro).
- Wu, F., Chen, J., and Zou, Q. (2019). A Nonlinear Creep Damage Model for Salt Rock. *Int. J. Damage Mech.* 28 (5), 758–771. doi:10.1177/1056789518792649
- Xie, H., Li, C., He, Z., Li, C., Lu, Y., Zhang, R., et al. (2021). Experimental Study on Rock Mechanical Behavior Retaining the *In Situ* Geological Conditions at Different Depths. *Int. J. Rock Mech. Mining Sci.* 138, 104548. doi:10.1016/j.ijrmms.2020.104548
- Yang, H. Q., Zeng, Y. Y., Lan, Y. F., and Zhou, X. P. (2014). Analysis of the Excavation Damaged Zone Around a Tunnel Accounting for Geostress and Unloading. *Int. J. Rock Mech. Mining Sci.* 69, 59–66. doi:10.1016/j.ijrmms.2014.03.003
- Yu, Y., Jiang, J., and Zhang, L. (2008). A New Distance Metric Learning Algorithm. *Inf. Electron. Eng.* 6, 115–119. doi:10.3969/j.issn.1672-2892.2008.02.009
- Yu, M., Yu, M., and Yu, M.-H. (2004). *Unified Strength Theory and its Applications*. Berlin: Springer.
- Zhang, L., Ba, J., Fu, L., Carcione, J. M., and Cao, C. (2019). Estimation of Pore Microstructure by Using the Static and Dynamic Moduli. *Int. J. Rock Mech. Mining Sci.* 113, 24–30. doi:10.1016/j.ijrmms.2018.11.005
- Zhang, Z. X., Kou, S. Q., Jiang, L. G., and Lindqvist, P.-A. (2000). Effects of Loading Rate on Rock Fracture: Fracture Characteristics and Energy Partitioning. *Int. J. Rock Mech. Mining Sci.* 37 (5), 745–762. doi:10.1016/s1365-1609(00)00008-3
- Zhao, J., Sun, J., Liu, X., Chen, H., and Cui, L. (2013). Numerical Simulation of the Electrical Properties of Fractured Rock Based on Digital Rock Technology. *J. Geophys. Eng.* 10 (5), 055009. doi:10.1088/1742-2132/10/5/055009
- Zhu, W. C., Bai, Y., Li, X. B., and Niu, L. L. (2012). Numerical Simulation on Rock Failure under Combined Static and Dynamic Loading during SHPB Tests. *Int. J. Impact Eng.* 49, 142–157. doi:10.1016/j.ijimpeng.2012.04.002
- Zienkiewicz, O. (1977). Some Useful Forms of Isotropic Yield Surfaces for Soil and Rock Mechanics. *Finite Elem. geomechanics*, 179–190.

Conflict of Interest: Author ZC is employed by China Petroleum Logging CO. LTD.

The remaining authors declare that the research was conducted in the absence of any commercial or financial relationships that could be construed as a potential conflict of interest.

Publisher's Note: All claims expressed in this article are solely those of the authors and do not necessarily represent those of their affiliated organizations, or those of the publisher, the editors and the reviewers. Any product that may be evaluated in this article, or claim that may be made by its manufacturer, is not guaranteed or endorsed by the publisher.

Copyright © 2022 Zhang, Sun, Cheng, Xin and Chen. This is an open-access article distributed under the terms of the Creative Commons Attribution License (CC BY). The use, distribution or reproduction in other forums is permitted, provided the original author(s) and the copyright owner(s) are credited and that the original publication in this journal is cited, in accordance with accepted academic practice. No use, distribution or reproduction is permitted which does not comply with these terms.